

## Evaluation of digital image correlation techniques using realistic ground truth speckle images

This article has been downloaded from IOPscience. Please scroll down to see the full text article.

2010 Meas. Sci. Technol. 21 055102

(<http://iopscience.iop.org/0957-0233/21/5/055102>)

View [the table of contents for this issue](#), or go to the [journal homepage](#) for more

Download details:

IP Address: 157.193.11.47

The article was downloaded on 21/08/2011 at 11:25

Please note that [terms and conditions apply](#).

# Evaluation of digital image correlation techniques using realistic ground truth speckle images

C Cofaru<sup>1</sup>, W Philips<sup>1</sup> and W Van Paepegem<sup>2</sup>

<sup>1</sup> Telin–IPI–IBBT, Ghent University, St-Pietersnieuwstraat 41, B-9000 Ghent, Belgium

<sup>2</sup> Department of Materials Science and Engineering, Ghent University, St-Pietersnieuwstraat 41, B-9000 Ghent, Belgium

E-mail: [Cornel.Cofaru@telin.ugent.be](mailto:Cornel.Cofaru@telin.ugent.be)

Received 3 November 2009, in final form 12 February 2010

Published 26 March 2010

Online at [stacks.iop.org/MST/21/055102](http://stacks.iop.org/MST/21/055102)

## Abstract

Digital image correlation (DIC) has been acknowledged and widely used in recent years in the field of experimental mechanics as a contactless method for determining full field displacements and strains. Even though several sub-pixel motion estimation algorithms have been proposed in the literature, little is known about their accuracy and limitations in reproducing complex underlying motion fields occurring in real mechanical tests. This paper presents a new method for evaluating sub-pixel motion estimation algorithms using ground truth speckle images that are realistically warped using artificial motion fields that were obtained following two distinct approaches: in the first, the horizontal and vertical displacement fields are created according to theoretical formulas for the given type of experiment while the second approach constructs the displacements through radial basis function interpolation starting from real DIC results. The method is applied in the evaluation of five DIC algorithms with results indicating that the gradient-based DIC methods generally have a quality advantage when using small sized blocks and are a better choice for calculating very small displacements and strains. The Newton–Raphson is the overall best performing method with a notable quality advantage when large block sizes are employed and in experiments where large strain fields are of interest.

**Keywords:** digital image correlation, speckle, interpolation, sub-pixel

## 1. Introduction

Experimental mechanics has been increasingly relying in recent years on motion estimation image processing techniques in obtaining full field displacement and strain fields. Under the general name of ‘digital image correlation (DIC)’, the approach has the advantages of being able to measure a wide range of displacements over the whole analyzed specimen area; it is a contactless method, meaning that the measurement process does not affect in any way the material behavior during tests and requires a relatively simple experimental setup. Over time, various DIC algorithms have been developed. Among these the most popular are those involving the cross-correlation coefficient and variations of the method for improving accuracy [1–3, 8, 9], the Fourier

transform [4–7], Newton–Raphson iterations [10–12] and gradient-based optical flow [14, 15]. The last two classes of algorithms present special interest because they are widely used and address differently two of the most important driving factors in algorithm development: computational performance and sub-pixel accuracy. As shown in [13], the Newton–Raphson methods have higher accuracy at the expense of computational complexity while gradient methods are faster.

One of the problems in evaluating the performance of DIC algorithms is that the artificial full-field displacement models used in the literature as ground truth to characterize specimen deformations may not reflect the variations encountered in real motion fields. Rigid body displacement, linear and quadratic displacement models [13, 16, 17] have been used, resulting in good approximation of the absolute accuracy

when the DIC algorithm motion model matched or was more complex than the full-field displacement model. To provide a better understanding of the advantages and limitations of the algorithms in practical applications, this paper proposes a new DIC evaluation method under more realistic but still reproducible circumstances through the use of a larger variety of realistic motion models and discontinuities, speckle patterns obtained by photographing spray-painted material specimens and a numerical deformation process that best simulates image intensity changes captured by real cameras. The paper is organized as follows: section 2 contains a short overview of the five DIC algorithms that are evaluated, section 3 presents the framework based on the radial basis function (RBF) theory used to create the ground truth motion fields and images, and finally sections 4 and 5 contain the results and conclusions of the DIC method evaluation, respectively.

## 2. Digital image correlation algorithms

The fundamental principle behind DIC algorithms is that motion information is extracted from speckle images that show a speckle painted mechanical test specimen before and after deformation, by minimizing a chosen similarity function between subsets or blocks of the images. In this paper we will focus the evaluation on the recovery of the sub-pixel or fractional part of the displacements only since integer pixel displacements are relatively easy to obtain through various block matching or coarse-to-fine approaches.

Considering a ‘reference’ and a ‘deformed’ block,  $f(x, y)$  and  $g(x', y')$  of size  $M \times M$ , occupying the same spatial coordinates inside the images that represent the specimen before and after deformation, the quadratic error measure between the two blocks is defined as

$$E(u(x, y), v(x, y)) = \sum_{x=1}^M \sum_{y=1}^M (f(x, y) - g(x', y'))^2 \quad (1)$$

with

$$x' = x + u(x, y) \quad (2a)$$

$$y' = y + v(x, y), \quad (2b)$$

where  $u(x, y)$  and  $v(x, y)$  are the sub-pixel horizontal and vertical displacements of the pixel located at the coordinates  $(x, y)$  in the reference block.

*Gradient DIC methods* rely on the assumption that for small displacements image intensity patterns remain unchanged between the reference and deformed images. The two methods evaluated in this paper rely on finding the solution for  $u(x, y)$  and  $v(x, y)$  that minimizes the error function from equation (1) by replacing  $g(x', y')$  with its first or second degree Taylor expansion and solving the resulting linear system through a *least-squares* approach. Depending on the complexity of the motion that is to be recovered, various motion models within the block can be assumed. Usually linear [18, 19] and rigid body displacement motion models are used. The solutions for the rigid body displacement model considering the two

Taylor expansions of the ‘deformed’ block are presented in appendix A.

The *Newton–Raphson method* approaches the minimization of equation (1) by gradual iterative convergence toward the error function’s minimum and usually is associated with more complex linear or quadratic [12] motion models for the intensity patterns inside the deformed blocks. Here, only the linear expression for the pixel displacements is considered. In practice, starting from an initial integer displacement solution, the algorithm iteratively warps through bicubic spline interpolation the reference block using the calculated motion parameters from the previous iteration until it becomes similar to the deformed block, thus minimizing the error between the two. The convergence criterion used here was a maximum difference of  $10^{-5}$  between each motion parameter in two consecutive iterations with convergence reached after two to four iterations. Because each iteration involves updating the Hessian of the error function they can be computationally expensive. This shortcoming can be avoided by using the approximation introduced by Vendroux [11] where the Hessian elements are calculated using only the first-order partial derivatives of the interpolated block with respect to the motion parameters.

*Robust methods* in the form proposed by Black and Anandan [20] seek to eliminate the disadvantage of using the quadratic error function as block similarity measure because its resulting motion estimate is equally influenced by all pixel motions inside the block. By using a robust error function such as M-estimators instead of the quadratic one, pixel locations that fit the overall motion are preferentially used in the final motion estimate. Consequently, the negative influence of image noise, motion outliers and multiple motions inside the block is limited. A popular choice for the robust estimator chosen also here is the Lorentzian with the general expression

$$\rho(x, \sigma) = \log \left( 1 + \left( \frac{x}{2\sigma} \right)^2 \right), \quad (3)$$

where  $\sigma$  is a parameter that controls the strength of the outlier rejection. To increase the spatial consistency of the motion field, a regularizing or smoothness term can be added to the data term associated with the intensity levels in the image. The criterion to be minimized in matching the two blocks becomes for a translational motion model with  $u(x, y) = u_0$  and  $v(x, y) = v_0$

$$E(u_0, v_0) = \lambda_D E_D(u_0, v_0) + \lambda_S E_S(u_0, v_0), \quad (4)$$

with

$$E_D(u_0, v_0) = \sum_{x=1}^M \sum_{y=1}^M \rho_D(f(x, y) - g(x + u_0, y + v_0), \sigma_D) \quad (5a)$$

$$E_S(u_0, v_0) = \sum_{i=1}^8 (\rho_S(u_0 - u_i, \sigma_S) + \rho_S(v_0 - v_i, \sigma_S)), \quad (5b)$$

where  $\lambda_D, \lambda_S$  are weights assigned to the data and smoothness terms  $E_D$  and  $E_S$ ,  $\rho_D, \rho_S$  and  $\sigma_D, \sigma_S$  are the associated robust error functions and corresponding parameters respectively and

$(u_i)_{i=1,8}, (v_i)_{i=1,8}$  the spatial neighbors in the motion fields of the horizontal and vertical displacements  $u_0$  and  $v_0$ .

To analyze the benefits and drawbacks of having a regularization term in the error function, we will evaluate two implementations: one with  $E_S$  present and one with it absent in  $E$ . The minimization of equation (4) through successive over-relaxation (SOR) and values for the method's parameters are detailed in appendix B.

### 3. Realistic ground truth

The main contribution of this paper is to propose a method to create generally realistic ground truth data for the evaluation of DIC algorithms by deforming real speckle images. The four ground truth images that will be used in the evaluation are generated using different artificial displacement fields obtained through two distinct approaches. In the first one, displacement fields are calculated from the theoretical modeling of stress and strain distributions in homogeneous materials under load. Three theoretical scenarios are employed: a bi-axially loaded infinite plate with a central hole presenting small and large strain deformations and the lateral localized application of a surface tension. All cases are of practical interest for DIC evaluation since they simulate the theoretical solution for frequently encountered experimental scenarios. The inplane motion has a large degree of spatial variation and the displacement magnitude can be easily modeled through the stress and material properties parameters. The second approach uses DIC results from real deformation tests to create image-sized artificial displacement fields through radial basis function interpolation providing a very flexible alternative to theoretical displacements as well as finite-element generated displacement fields [21]. This results in deformation fields close to those encountered in mechanical experiments but of course has the disadvantage that it suffers from the artifacts generated by the measurement method. Experimental relevance of the motion data in this case is assured through the choice of the test setup from which motion data are extracted and of the DIC algorithm parameters used to extract it. The realistic nature of the ground truth is reflected also in the image intensity levels by choosing the interpolation method that guarantees the best reproduction of deformed speckle images acquired by the camera. This differs from other approaches that seek the best interpolation method for simulating the sub-pixel intensity pattern movements because the principal goal of the evaluation is to replicate as much as possible the real experimental data and not to simulate ideal experimental conditions.

The chosen size for the ground truth images and implicitly all generated artificial motion fields is  $1024 \times 1024$  pixels as it is a resolution easily attainable by modern digital cameras and provides, correlated with the block sizes chosen for the DIC algorithms, a reasonable amount of motion information for the statistical relevance of the results.

#### 3.1. 'Plate with hole' model

The solution for the inplane displacements of an infinite isotropic plate with a hole bi-axially loaded as shown

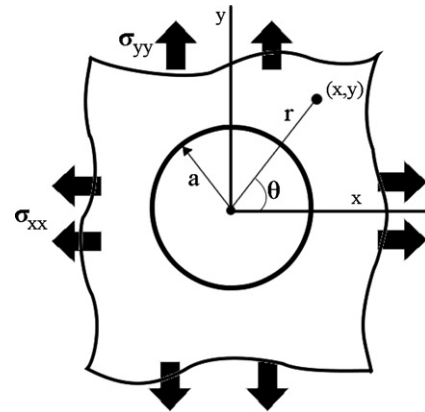


Figure 1. Bi-axial loading of an infinite plate with a hole.

schematically in figure 1 can be obtained by applying the superposition principle for the Kirsch solution in the case of uniaxial stress. This results in the following expressions for the radial and tangential polar coordinate displacements  $u^{(p)}$  and  $v^{(p)}$  respectively [22]:

$$u^{(p)}(x, y) = \frac{1}{2E} [(A + B \cos 2\theta)\sigma_{xx} + (A - B \cos 2\theta)\sigma_{yy}] \quad (6a)$$

$$v^{(p)}(x, y) = \frac{1}{2E} C(\sigma_{xx} - \sigma_{yy}) \sin 2\theta \quad (6b)$$

with the terms  $A$ ,  $B$  and  $C$

$$A = r(x, y)[(1 - \nu) + (1 + \nu)c^2(x, y)] \quad (7a)$$

$$B = r(x, y)[4c^2(x, y) + (1 + \nu)(1 - c^4(x, y))] \quad (7b)$$

$$C = -r(x, y)[(1 + \nu) + 2(1 - \nu)c^2(x, y) + (1 + \nu)c^4(x, y)], \quad (7c)$$

where  $E$  is the elasticity modulus,  $\nu$  is Poisson's ratio,  $a$  is the radius of the hole,  $r(x, y)$  is the distance from the point of interest located at  $(x, y)$  to the center of the hole,  $c = a/r$ ,  $\theta$  is the angle of the point of interest with respect to the  $x$  axis and  $\sigma_{xx}, \sigma_{yy}$  are the stresses applied in the directions consistent with the horizontal and vertical directions. The horizontal and vertical displacements can be obtained from equation (6a) and equation (6b) with a transformation of the form

$$u(x, y) = u^{(p)}(x, y) \cos \theta - v^{(p)}(x, y) \sin \theta \quad (8a)$$

$$v(x, y) = u^{(p)}(x, y) \sin \theta + v^{(p)}(x, y) \cos \theta. \quad (8b)$$

In figure 2 the typical contours of the artificial horizontal and vertical displacements are illustrated with material properties  $E = 210$  GPa,  $\nu = 0.25$  corresponding to steel,  $a = 200$  pixels and stresses  $\sigma_{xx} = 50$  MPa,  $\sigma_{yy} = 350$  MPa.

#### 3.2. 'Concentrated lateral surface tension' model

Applying force on a very small surface on the edge of a solid isotropic body in a horizontal direction generates a highly localized surface tension and stress area around the

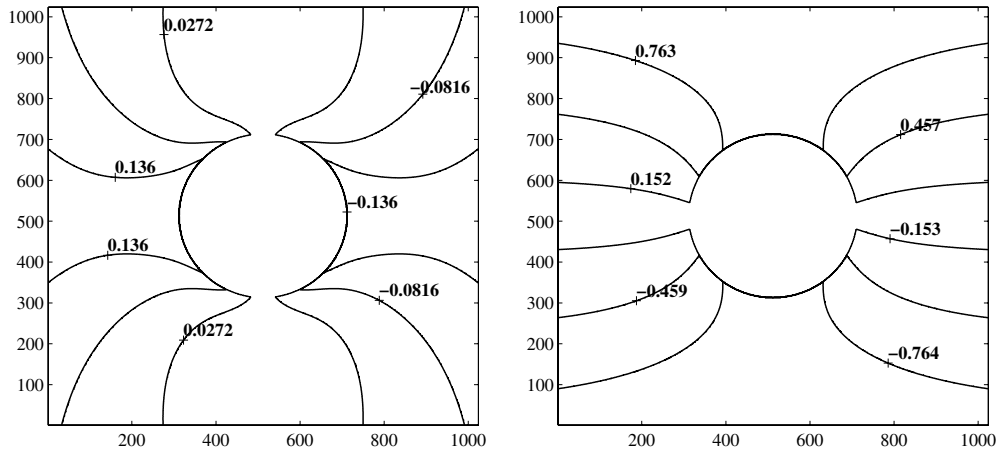


Figure 2. Horizontal (left) and vertical (right) displacement contours for the ‘plate with hole’ displacement model.

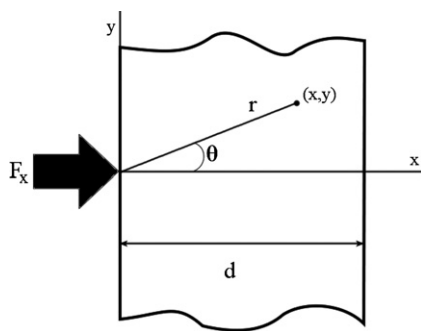


Figure 3. Concentrated lateral tension.

point of application. For the scenario indicated in figure 3, the following expressions [23] for the inplane horizontal and vertical displacements based on the solution for the ‘Flamant problem’ can be obtained:

$$u(x, y) = -\frac{2F_x}{E\pi} \left( \ln \frac{r(x, y)}{d} + \frac{1 + \nu}{2} \sin^2 \theta \right) \quad (9a)$$

$$v(x, y) = \frac{F_x}{E\pi} [(1 + \nu) \sin \theta \cos \theta - (1 - \nu)\theta], \quad (9b)$$

where  $E$  is the elasticity modulus,  $\nu$  is Poisson’s ratio,  $F_x$  is the lateral surface tension,  $r(x, y)$  is the distance from the point of interest located at  $(x, y)$  to the stress application point,  $\theta$  is the angle of the point of interest with respect to the  $x$  axis and  $d$  is the width of the material. In obtaining these particular solutions, the vertical displacements along the stress application direction and the horizontal and vertical displacements at the right edge of the body are considered zero as boundary conditions. The contours of the artificial horizontal and vertical displacements are shown in figure 4 for a lateral surface tension  $F_x = 420 \text{ kN m}^{-1}$  present on the left edge of the specimen and considering the material to be steel with the same properties as in section 3.1. Because the horizontal displacements are highly localized, only a detail of the whole horizontal displacement field is shown.

### 3.3. Deformation fields extracted from DIC measurements

In many cases where DIC algorithms are being employed, little or no theoretical background information exists on the behavior of the analyzed material specimen and thus no theoretical formulas of the underlying displacement fields can be formulated. It is therefore necessary to rely on the DIC results to create artificial motion fields tailored to specific experiments. The influence of outliers from the experimental motion data, caused by lighting variations, imperfections in the speckle pattern, camera noise and the numerical approach of the DIC algorithm, can be minimized in the creation of the artificial motion fields by using only a subset of the motion information, distributed on a sparse grid. A second observation to suggest the use of a sparse grid is that the largest parts of the motion fields are smoothly varying and necessitate less information for the interpolation process resulting in both smoother artificial displacements and increased interpolation speed.

Radial basis functions have been extensively used for sparse data interpolation in a wide range of fields, from facial expression recognition and medical imaging to mechanical and aeronautical applications [24–32], which makes their choice appropriate in the creation of the ground truth motion fields. The basic principle behind RBF interpolation is that each interpolated value can be expressed as a weighted sum of the values from known data locations with the weighing factor in direct proportion to a function of the Euclidean distances between the known and interpolated locations. Various radial basis functions  $\Phi$  are used in the literature depending on the application field, this paper investigating the usage of four functions:

- linear:  $\Phi(x) = x$ ;
- cubic:  $\Phi(x) = x^3$
- multiquadric:  $\Phi(x) = \sqrt{x^2 + c^2}$
- thinplate spline:  $\Phi(x) = x^2 \log(x)$ ,

where, if present, the parameter  $c$  controls the shape of the basis function. The theoretical aspects of solving the interpolation problem for a given radial basis function are presented in appendix C. Since the artificially generated displacements

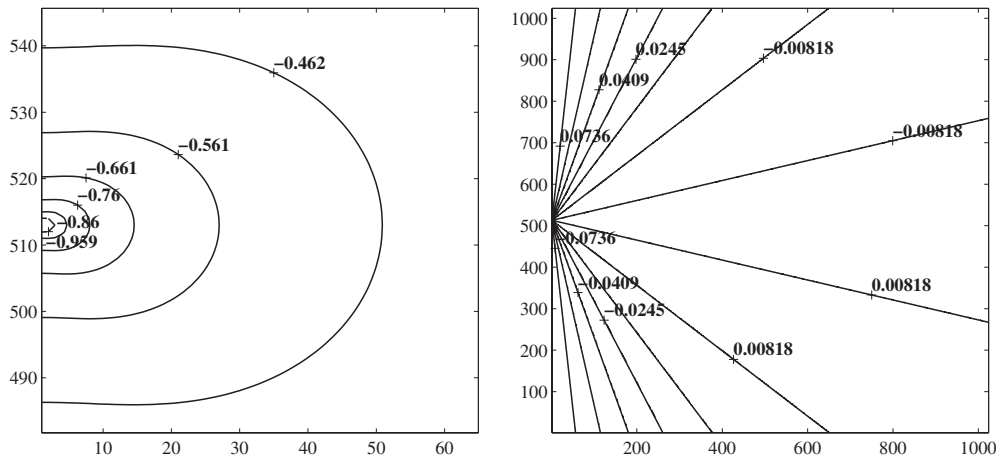


**Figure 4.** Detail of the horizontal (left) and vertical (right) displacement contours for the ‘concentrated lateral tension’ displacement model.

represent the new ground truth, they do not need to perfectly reproduce the underlying real displacements but instead to create an experimentally relevant simulation of the material deformation. This permits the usage of any of the radial basis functions depending on the desired or assumed spatial variation of the motion and adds to the flexibility of the method as it allows pre-processing of the initial data with the scope of increasing its reliability.

To create the sparse grids for the displacement interpolation an adaptive quadtree partitioning scheme similar to that found in [25] is used to adaptively select locations from the initial motion fields to be used as known data points in the displacement interpolation process: after starting with an initial regular grid, at each step, data are interpolated using the resulted adaptive grid from the previous step. The errors between the initial displacement data and the interpolant are evaluated in neighboring locations situated at half node distance around nodes specifically selected in the previous step. If at a certain location the error is smaller than a chosen ‘coarsening’ limit  $\varepsilon_C$ , that location will not be added on the grid. Otherwise, the location is added and the error is compared to a ‘refining’ limit  $\varepsilon_R$ : if the error is larger than this limit, the neighbors will be used in the error evaluation for the next iteration interpolant. The limits  $\varepsilon_C$  and  $\varepsilon_R$  are adaptively calculated to keep constant at each iteration the percentages of points that are eliminated or whose neighbors will be investigated. Vertical displacements may exhibit different spatial variations from the horizontal ones, both in amplitude and frequency, thus the selection algorithm is applied separately for the horizontal and vertical displacements in order to adequately capture variations in each direction and stops when the distance between a node on the grid and its neighbors is smaller than 1. For numerical stability, as noted in [25], adaptation of the shape parameter  $c$  for the multiquadric RBF (which is initialized with the mean distance between two neighboring nodes of the initial regular grid) is done by halving its value at each iteration.

The initial motion data for the artificial displacements came from an earlier experiment [7] in which a plastic glass security film with three central holes is subjected to uniaxial

vertical stress in an upward direction. The Newton–Raphson DIC method with a block size of  $16 \times 16$  pixels, no overlapping between blocks and a linear motion model is used to obtain the horizontal and vertical motion fields. The block size chosen offered a good compromise between accuracy and spatial resolution: the use of a smaller block size would necessitate additional processing of the motion fields as the number of outliers would be very large while larger block sizes would result in severe smoothing of the discontinuities present. The contours of the initial motion fields of size  $64 \times 64$  after being filtered with a  $3 \times 3$  median filter for gross outlier removal are shown in figure 5.

As can be noticed from the contours, motion variations on the horizontal direction are quite small and with a large degree of noise while vertical displacements exhibit a large discontinuity in the central area due to the presence of the holes. For the motion interpolation procedure the multiquadric RBF was used with an initial grid of  $6 \times 6$  locations and the limits  $\varepsilon_C$  and  $\varepsilon_R$  set to 1% and 12% of the total number of new locations added in the current iteration. The contours of the resulting artificial motion fields are presented in figure 6. In total, 284 locations were used for the horizontal displacement and 263 for the vertical respectively which account for less than 7% out of the total number of 4096 locations. The result of the interpolation procedure was the smoothing of large parts of the motion fields while maintaining the typical amplitudes. An undesired effect is the enlargement of the central discontinuity in the vertical displacements in direct proportion to the zoom factor imposed by resizing the dataset to image size, in this case the block size of the N-R algorithm used to obtain the motion data. The undesired smoothing effect can be compensated for by either choosing a smaller block size for the motion estimation algorithm or adaptively smoothing the motion field directly with an edge enhancing operator like anisotropic diffusion [33]. Here, no post-processing of the motion fields is done as the gradient magnitude is large taking into consideration the block sizes used in the evaluation of the DIC methods.

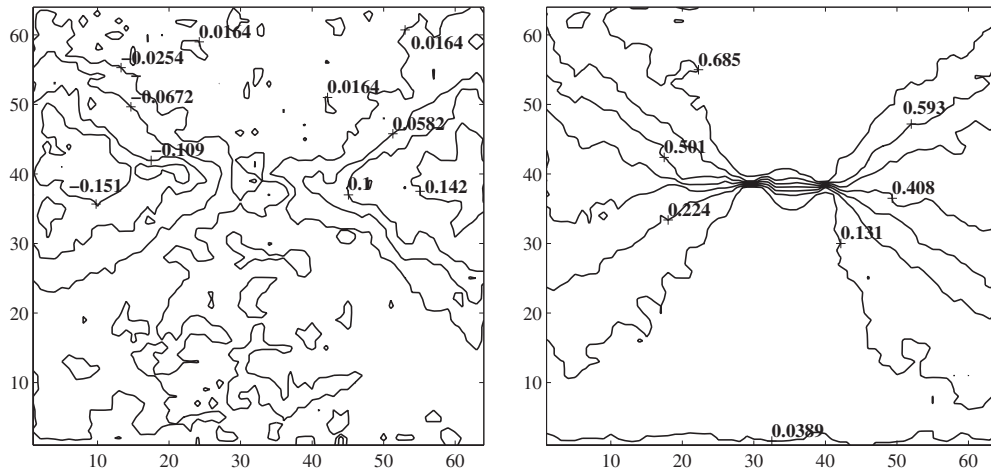


**Figure 5.** Horizontal (left) and vertical (right) displacement contours for the initial motion data used in interpolating artificial displacements.

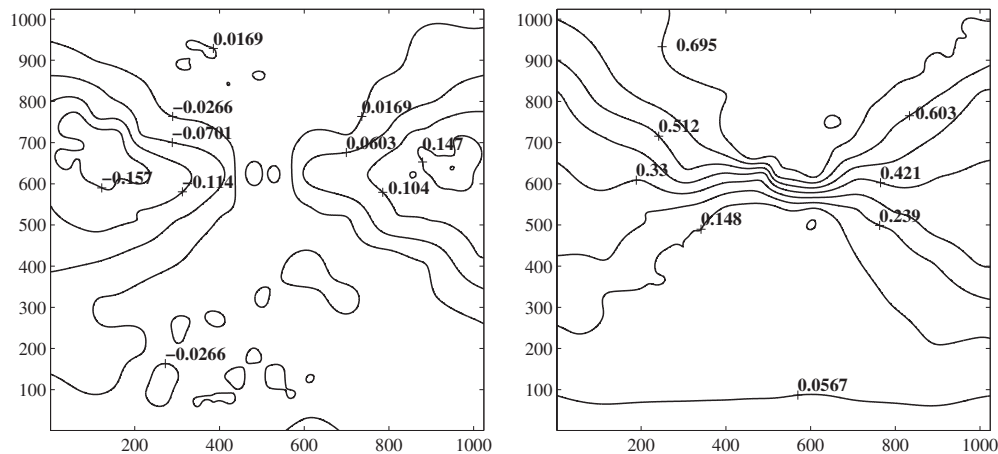


**Figure 6.** Horizontal (left) and vertical (right) displacement contours of the interpolated image sized artificial displacements.

### 3.4. Image warping

The speckle patterns used in the ground truth images were photographed with a Pixelink PL-A782 camera at a resolution of  $2208 \times 3000$  pixels. Only the central  $1024 \times 1024$  pixel region was used in the warping process. The mechanical setup resulted in a pixel size of  $8.33 \mu\text{m}$  in the object plane. Creating the speckle pattern consisted of first painting the specimen white and subsequently spray painting it with black paint. Direct application of the paint on the specimen surface resulted in unfeasibly large speckles, so instead, the spray paint was applied on a surface near the specimen allowing only very small paint particles to settle to the specimen itself. This resulted in a random speckle pattern with speckle sizes ranging from 2 to 20 pixels in diameter or  $16.6$  to  $170 \mu\text{m}$  respectively. Prior to taking photographs of the specimen, the camera was aligned with a laser perpendicular to the specimen to avoid any out-of-plane displacements and calibrated through the proprietary software to compensate any lighting variation across the material surface, fixed-pattern noise and photo-response nonuniformities. The experimental setup used and the resulting speckle pattern are shown in figure 7.

The radial basis function interpolation framework is further investigated in creating the four ground truth speckle

images once the artificial motion fields are obtained. Because of the high frequency nature of speckle images, expressing a pixel's intensity as a weighted sum of neighboring pixels as the RBF theory implies can be achieved more efficiently by using only highly local information. The interpolation procedure starts by dividing the reference speckle image into blocks and subsequently warping each of them individually, according to the corresponding displacements for each pixel. Additional pixels on the borders of the blocks are added to eliminate any interpolation artifacts near the block borders, the number added depending on the magnitude of the displacements. In the case of all the tests performed here, borders two pixels in width are used. After interpolation, to simulate the quantization process of a real camera, the resulting real-valued gray levels are quantized to 8 bit integers. Considering a  $3 \times 3$  block with a border one pixel in width in the reference image as shown in figure 8, obtaining the intensities of each individual pixel location in the warped block is done by interpolating the intensity at the location opposite from where the motion vector indicates the intensity pattern will move.

To analyze the interpolation quality of the interpolation method, a rigid body displacement registration test is employed. The specimen containing the speckle pattern

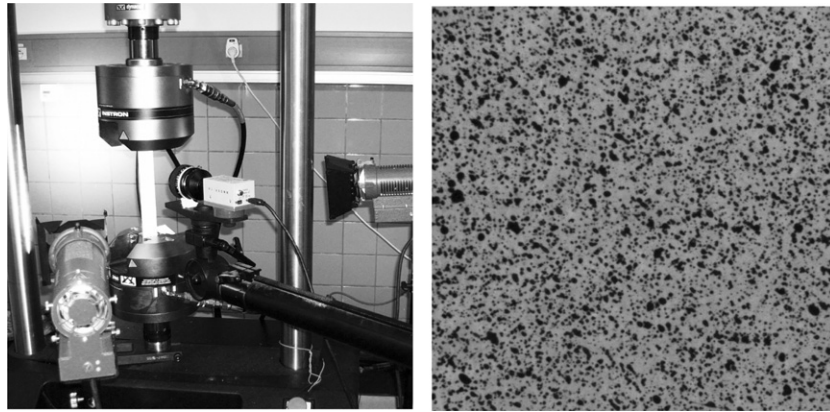


**Figure 7.** Experimental setup (left) and speckle pattern used to create the ground truth images (right).

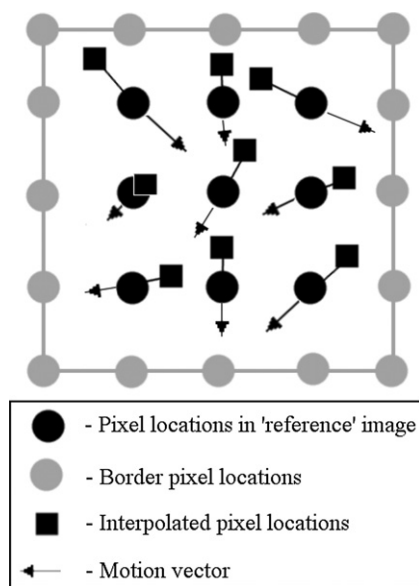


**Figure 8.** Image warping process for a  $3 \times 3$  pixel block (its actual size is  $5 \times 5$  because of the border pixels used only for interpolation): pixel intensities at the locations indicated by the dark circles in the reference block are replaced in the warped block by the corresponding interpolated intensities indicated by the squared locations.

is translated using a Instron 8801 servohydraulic machine  $50 \mu\text{m}$  in steps of  $10 \mu\text{m}$  corresponding to 1.2 pixels and pictures taken before and after each translation step. The camera was triggered electronically so that the effect of vibrations could be kept to a minimum and not affect the calibration. Since only the central  $1024 \times 1024$  pixel central area is analyzed, the integer pixel displacements can be easily compensated without loss of information at its borders so that only the sub-pixel displacements remain present, resulting in displacements of 0.2, 0.4, 0.6, 0.8 and 1.0 pixels for the five displaced pictures. The image of the specimen before translation is warped to simulate the five displacements and the root mean square error (RMSE) between it and the real displaced pictures is calculated. Additional comparisons are done by warping the second, third and fourth displaced pictures and comparing them to

the subsequent four, three and two pictures in the sequence. Bicubic and bicubic spline are included along with the RBF interpolation methods in the evaluation to provide a quick quality reference. The results are shown in figures 9(a), (b), (c) and (d), respectively. The chosen block size for the RBF interpolation was  $8 \times 8$  pixels with the mention that insignificant quality differences were noticed when varying the dimensions between  $3 \times 3$  and  $32 \times 32$  pixels.

The results clearly indicate that the best registration quality is given by the linear RBF followed by bicubic interpolation. This might be due to the fact that the linear weighted averaging in which the pixel intensities are calculated is similar to the process in which the camera system calculates the intensity of a given element in the CCD sensor array. Since the goal is to reproduce as accurately as possible pictures taken by the camera, all the warped ground truth images used in the DIC evaluation will be generated using the linear RBF interpolation and the block size kept constant at  $8 \times 8$  pixels.

#### 4. DIC method evaluation

The evaluation of the five DIC methods consists in using them to calculate the displacements and strains between the reference and the four artificially deformed ground truth speckle images. Block sizes of  $32 \times 32$ ,  $48 \times 48$  and  $64 \times 64$  pixels with a 16 pixel step size between blocks are used in the three test cases that refer to small strains. In evaluating the displacement errors, to take advantage of the fact that the motion is known for each pixel location, the displacement fields computed by each method are resized to the image size: where the translational displacement model was considered, all pixel locations from the block that contributed to the same displacement are assigned the computed value while for the linear model, all calculated parameters are used. The software implementation and tests were realized in the 64-bit version of Matlab on a 2.0 GHz Intel Core 2 Duo processor with 4 GB of RAM running the Linux operating system.

The displacement analysis takes into consideration the mean and standard deviation of the horizontal and vertical motion errors calculated between the ground truth motion fields and the DIC results after the resizing operation.

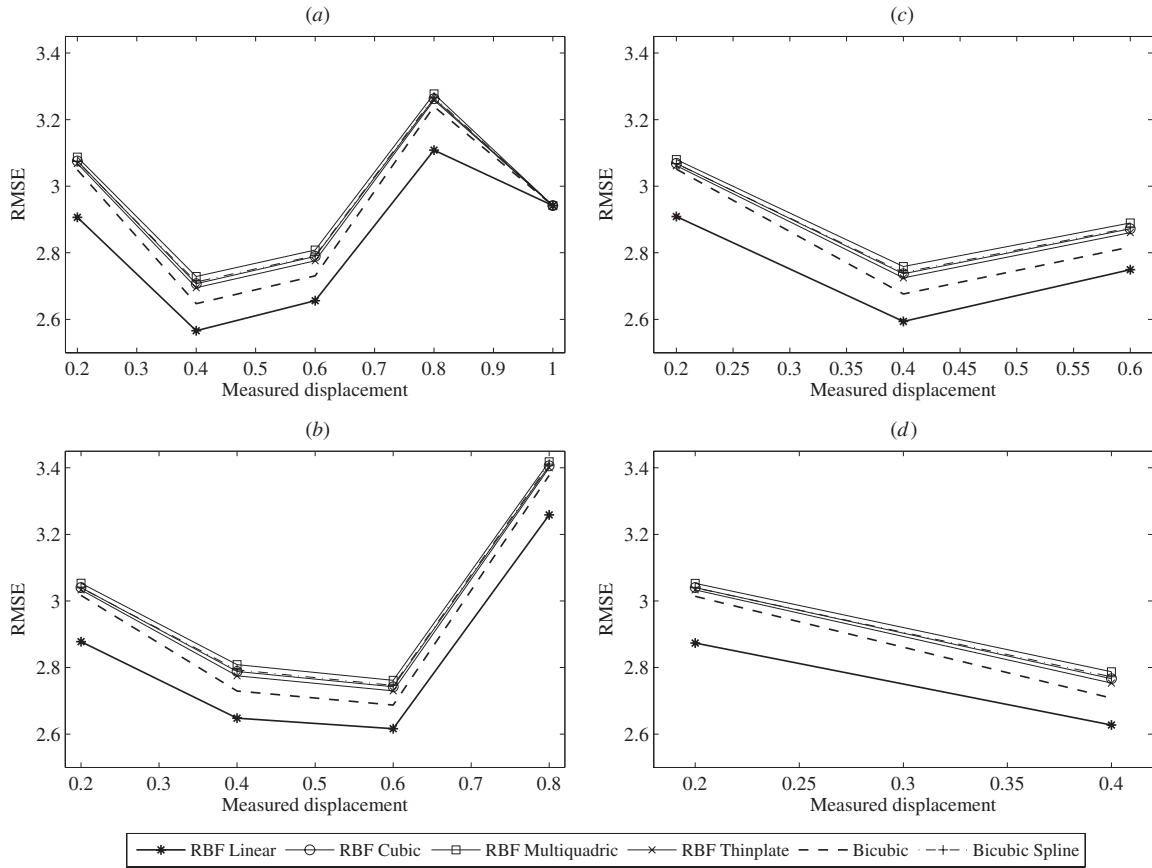


**Figure 9.** Mean square error between registered and displaced speckle images.

Considering the motion error  $e(x, y)$  at the location  $(x, y)$  in either the horizontal or vertical motion fields of size  $N \times N$ :

$$e(x, y) = u_{th}(x, y) - u_{DIC}(x, y), \quad (10)$$

where  $u_{th}(x, y)$  and  $u_{DIC}(x, y)$  are the theoretical and calculated displacements, and the mean error and standard deviation are defined as

$$\bar{e} = \frac{1}{N^2} \sum_{x=1}^N \sum_{y=1}^N e(x, y) \quad (11)$$

and

$$\sigma_e = \sqrt{\frac{1}{N^2 - 1} \sum_{x=1}^N \sum_{y=1}^N (e(x, y) - \bar{e})^2}, \quad (12)$$

respectively.

The error analysis will concentrate on both the full field errors and on the errors located in the image regions with strong discontinuities in the motion field. For the ‘plate with hole’ model, these regions correspond to a  $600 \times 600$  area around the hole located in the center of the image, for the ‘concentrated lateral tension’ model to a  $300 \times 300$  pixel area in the middle-left part of the image where the force is applied and for the ‘DIC measurement based’ displacements, the central  $400 \times 400$  pixel area.

The strain error analysis consists in calculating the mean of the absolute strain errors between the theoretical and the DIC measured strains in the locations corresponding to the

centers of each motion estimation block. The errors are calculated separately for the horizontal, vertical and shear strain components  $\varepsilon_{xx}$ ,  $\varepsilon_{xy}$  and  $\varepsilon_{yy}$ , respectively. Obtaining the strain for a certain location is done through a linear fit of the horizontal and vertical displacements inside a strain window of  $11 \times 11$  displacement values centered upon the location where the strain is desired, an approach found also in [34]. Special attention has been given to eliminating from the evaluation the locations that produce large false strains due to the absence of motion, like the immediate surroundings of the hole in the plate with the hole model. The resulting calculated strain and absolute error fields had the dimensions of  $53 \times 53$ ,  $52 \times 52$  and  $51 \times 51$  data points for DIC block sizes of  $32 \times 32$ ,  $48 \times 48$  and  $64 \times 64$  pixels, respectively.

#### 4.1. ‘Plate with hole’ model errors

Figure 10 presents the mean full-field errors and standard deviations in the form of error bars for the ‘plate with hole’ model. The vertical axis addresses the magnitude of the error and standard deviation measured in pixels. The DIC methods analyzed are represented on the horizontal axis where the abbreviations ‘G-I’, ‘G-II’, ‘N-R’, ‘R’ and ‘R-S’ stand for the two gradient methods with first and second degree Taylor expansions, the Newton–Raphson, robust and robust with smoothing term methods, respectively. Clearly the Newton–Raphson method produces the best results both in terms of mean error and in terms of standard deviation of the error,

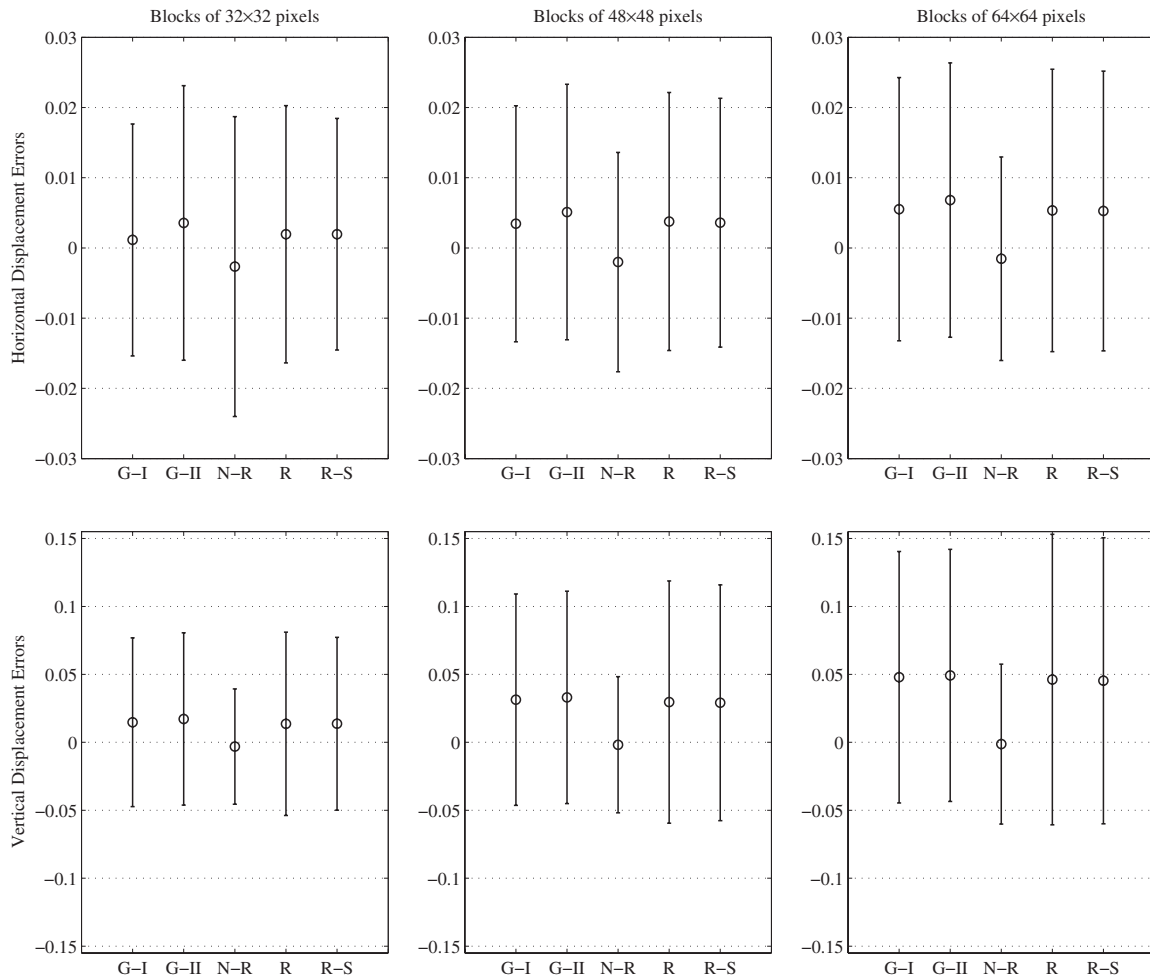


**Figure 10.** Mean error and standard deviation of the horizontal and vertical displacements for the ‘plate with hole’ displacement model.

the only exception being the horizontal errors for  $32 \times 32$  pixel block sizes where the first gradient method performs better. Increasing the block size produces a degradation of the quality for all methods except the Newton–Raphson one which performs better, most likely because the block size favors the accurate determination of the linear motion parameters compared to the other methods where the translational model clearly does not accurately describe the motion inside the larger block. The robust methods performed better than the gradient ones, the one including the smoothing term having a slight advantage in quality. Analysis of the errors in the  $600 \times 600$  pixel central area shown in figure 11 reveals larger errors and standard deviations for all methods and confirms the previous observations, with the Newton–Raphson mean errors being up to one order of magnitude smaller than those of the other algorithms.

The theoretical strains associated with the displacements fields presented variations between  $1.2 \times 10^{-3}$  and  $-6.86 \times 10^{-4}$  for  $\varepsilon_{xx}$ ,  $2.8 \times 10^{-3}$  and  $-2.8 \times 10^{-3}$  for  $\varepsilon_{xy}$  and  $4.7 \times 10^{-3}$  and  $1.73 \times 10^{-5}$  for  $\varepsilon_{yy}$ . In figure 12, the mean of the absolute strain errors are presented for the tested DIC methods. The main observation is that larger block sizes affect the quality of the strain fields probably because the motion model is too simple considering the areas covered in the image and

their underlying variations. For the horizontal strains, which are on average smaller, the gradient methods performed best; however, they exhibited poor performance for the shear and vertical strains. In these cases the Newton–Raphson method consistently produced the smallest errors. Strains larger than a lower limit of  $150\text{--}200 \mu\varepsilon$  were calculated by all methods with an accuracy of 15% or better, as the strain amplitude increased. The only notable exception was found in the immediate vicinity of the central hole for the shear strain errors with the largest strain errors varying from 50% to over 100% depending on the DIC method. This is mainly due to the fact that strains in these regions are extremely localized. Also, fewer displacement values are available for strain estimation when the strain window partially covers the hole because these locations are automatically excluded. Practical applicability of the DIC methods can however be improved in the regions near the hole through a more thorough block, step and strain window size optimization.

#### 4.2. ‘Concentrated lateral tension’ model errors

The results for the second test case presented in figure 13 show that the best quality is obtained by the gradient methods except when using  $64 \times 64$  blocks for the horizontal displacements

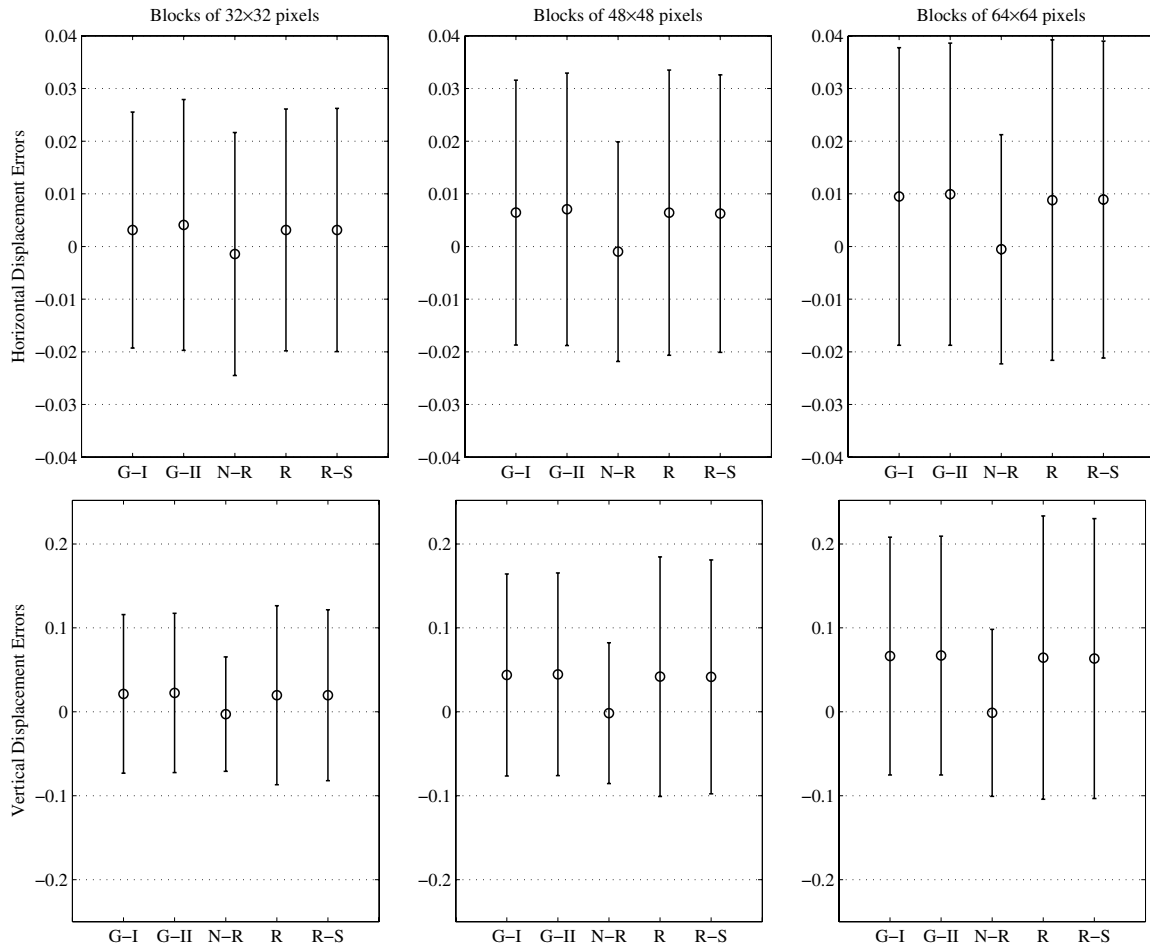


**Figure 11.** Mean error and standard deviation of the horizontal and vertical displacements for the ‘plate with hole’ displacement model in a  $600 \times 600$  pixel area around the central hole.

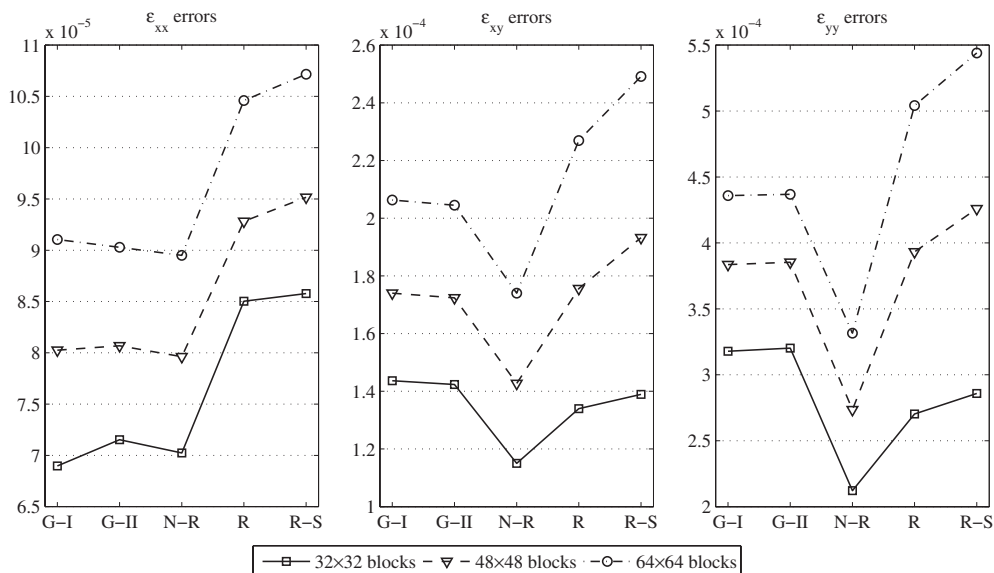


**Figure 12.** Mean of the absolute strain errors for the ‘plate with hole’ displacement model.

which present the strong lateral discontinuity. Interestingly, the mean error of  $-0.0064$  pixels for the gradient methods using  $32 \times 32$  pixel blocks is lower than the Newton–Raphson method error of  $-0.0088$  pixels obtained when using

$64 \times 64$  pixel blocks. The largest errors as well as standard deviations in the case of the horizontal displacements are given by the robust methods because they treated the highly localized motion as outliers and discarded the information

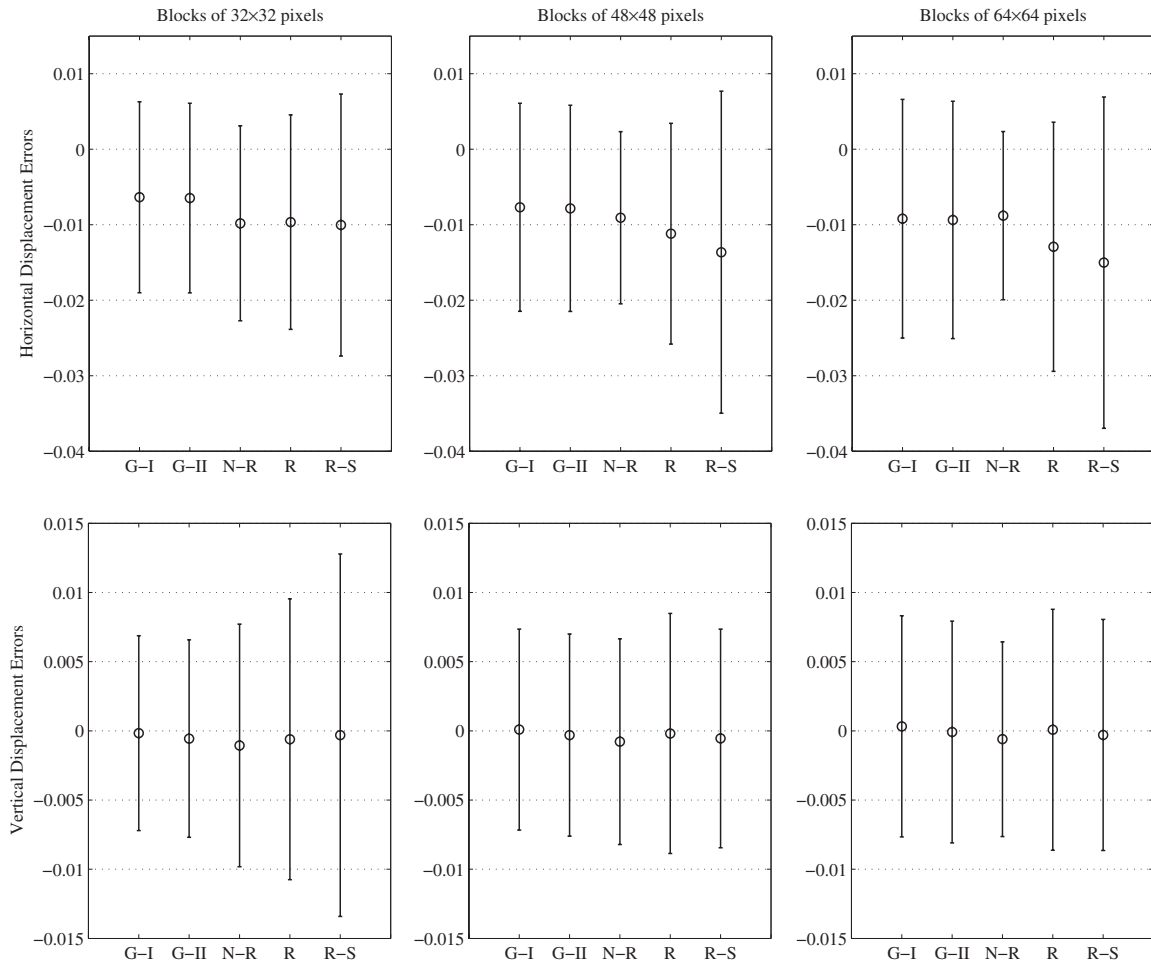


**Figure 13.** Mean error and standard deviation of the horizontal and vertical displacements for the ‘concentrated lateral tension’ displacement model.

from the pixels with large displacements. For the vertical displacements, which have an amplitude less than 0.1 pixels, both gradient and robust methods outperformed in terms of the mean error the Newton–Raphson method for all three block sizes, their errors being up to one order of magnitude smaller. Considering only the  $300 \times 300$  pixel region around the main horizontal motion discontinuity, the results shown in figure 14 indicate that the lowest horizontal and vertical errors for blocks sized  $32 \times 32$  and  $48 \times 48$  pixels are given by the gradient method containing the first degree Taylor expansion while for the block sized  $64 \times 64$  pixels, the Newton–Raphson method yields the lowest errors albeit significantly larger standard deviation. Also, as previously noticed for this case, the absolute error is smaller when using the gradient methods and smaller block sizes compared to the Newton–Raphson method and larger block sizes.

The ‘concentrated lateral tension’ model theoretical strains varied between  $2 \times 10^{-5}$  and  $-1.6 \times 10^{-3}$  for  $\epsilon_{xx}$ ,  $7.95 \times 10^{-4}$  and  $-7.95 \times 10^{-4}$  for  $\epsilon_{xy}$  and  $3.975 \times 10^{-4}$  and  $-3.975 \times 10^{-4}$  for  $\epsilon_{yy}$ . The strain errors from figure 15 indicate that choosing  $64 \times 64$  blocks yields the lowest strain errors; however, the error values vary very little when changing block sizes. This is mostly because the largest part of each of the three strain fields has very little underlying

strain variation with strains generally smaller than  $300 \mu\epsilon$ . The same lower limit of reliability applies also in this case, with strains of absolute value less than  $200 \mu\epsilon$  presenting errors in excess of 15%. This limit becomes much larger or approximately  $500 \mu\epsilon$  for the strains located near the lateral tension application because of the obvious large differences between the zero- or first-order displacement models used by the DIC algorithms and the theoretical displacement variations. The horizontal strain results are even more affected by strain discontinuities with the errors corresponding to largest strain values ranging from 26% in the case of the gradient methods and  $32 \times 32$  blocks size to 82% for the robust method with smoothing term and  $64 \times 64$  blocks. It is clear that in tests which present a very high localization of strains it is important to keep block sizes and strain window sizes as small as possible while ensuring that the information contained in each suffices for accurate motion and strain estimates.

#### 4.3. ‘DIC-based’ displacement model errors

The horizontal DIC errors from the last of the test images, shown in figure 16, indicate that the gradient method with a second degree Taylor expansion has the smallest errors for blocks of size  $32 \times 32$  and  $48 \times 48$  pixels. The

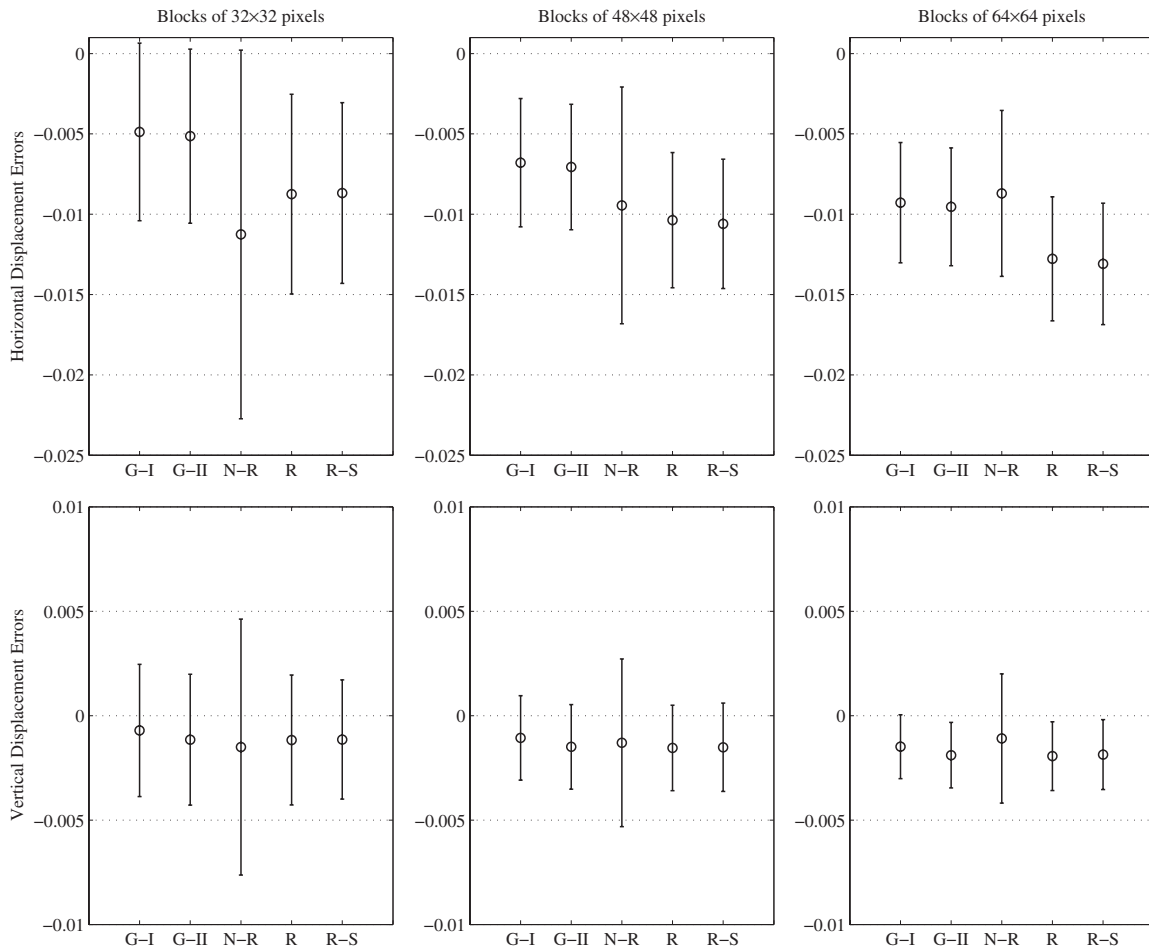


**Figure 14.** Mean error and standard deviation of the horizontal and vertical displacements for the ‘concentrated lateral tension’ displacement model in a  $300 \times 300$  pixel area around the lateral stress application point.

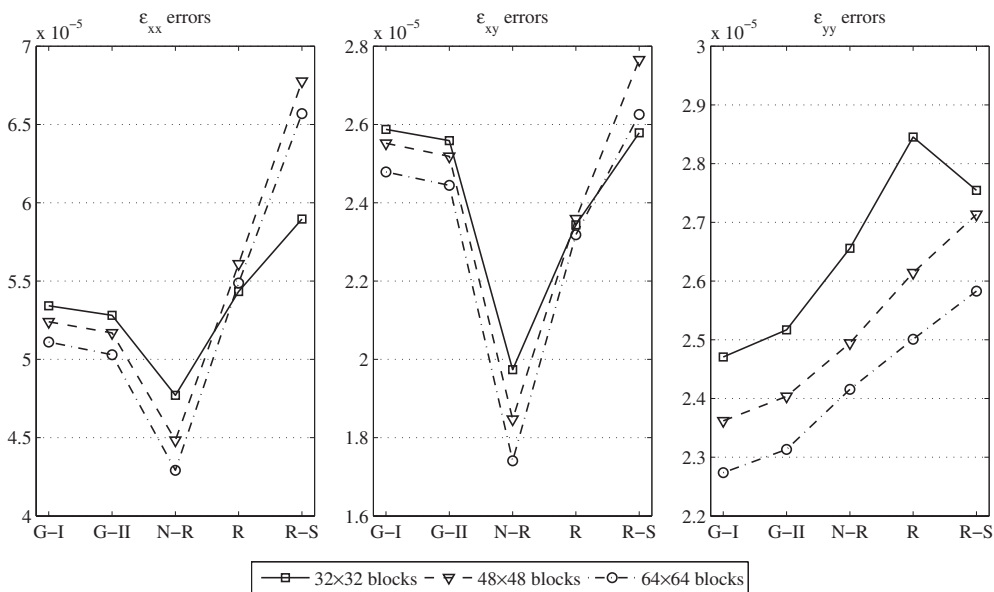


**Figure 15.** Mean of the absolute strain errors for the ‘concentrated lateral tension’ displacement model.

Newton–Raphson method presents the lowest horizontal errors and standard deviations for the  $64 \times 64$  pixel blocks and for all block sizes in the case of the vertical displacements. The robust

methods have comparable performance with the gradient ones for the smoother horizontal displacements and perform better for the vertical displacements except when using  $64 \times 64$

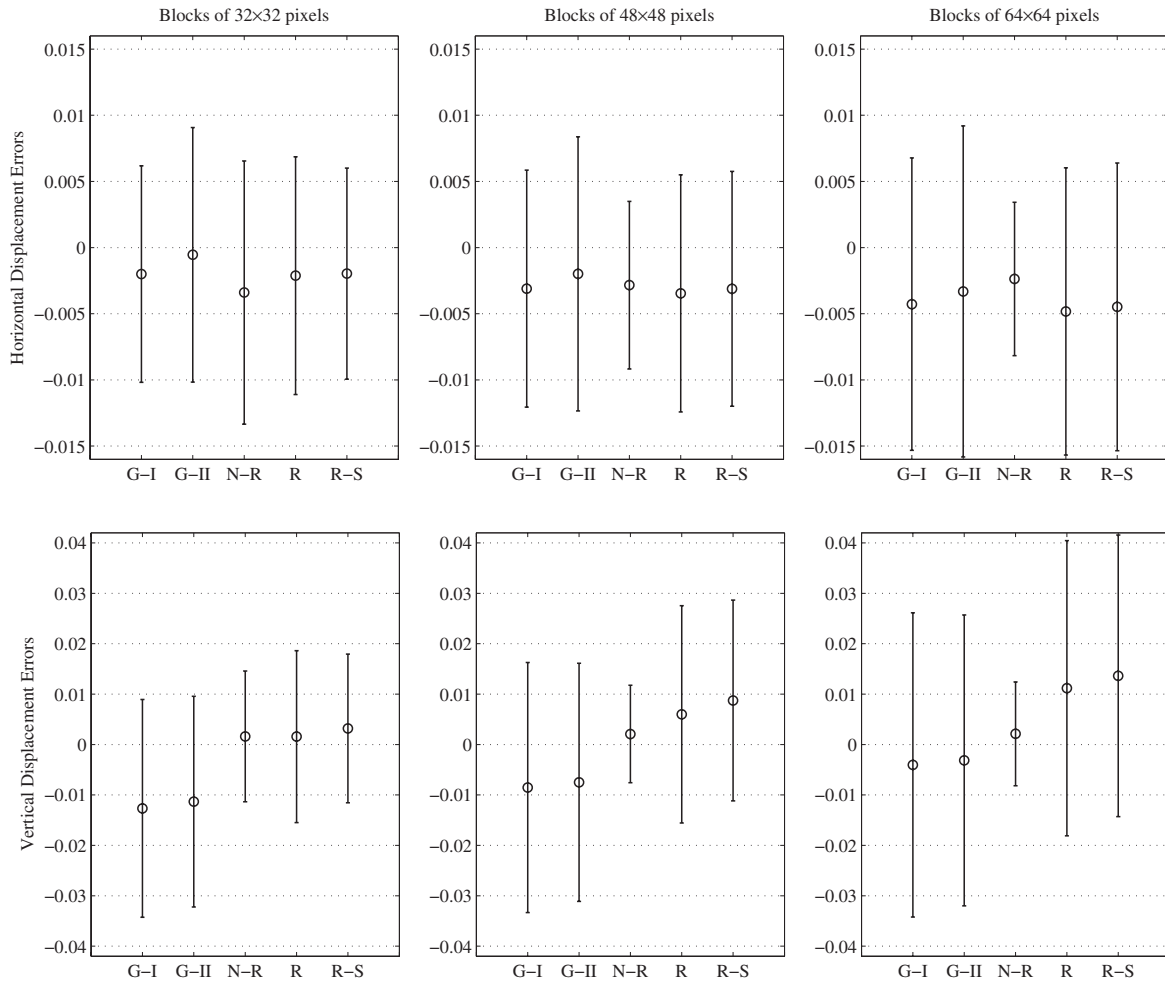


Figure 16. Mean error and standard deviation of the horizontal and vertical displacements for the ‘DIC-based’ displacement model.

blocks. Errors in the  $400 \times 400$  pixel central region of the image presented in figure 17 indicate the same quality pattern with gradient methods performing better at lower block sizes and their overall quality inversely proportional to the block size while the Newton–Raphson method benefits significantly from the increase in block size and gives the best overall quality at blocks over  $48 \times 48$  pixels. Here, as in the first case analyzed, performance advantage of the Newton–Raphson was more apparent where the absolute displacement magnitude was larger, namely in the case of vertical displacements.

The ‘DIC-based’ model theoretical strains varied between  $4.0 \times 10^{-3}$  and  $-2.4 \times 10^{-3}$  for  $\epsilon_{xx}$ ,  $1.8 \times 10^{-3}$  and  $-3.6 \times 10^{-3}$  for  $\epsilon_{xy}$  and  $7.8 \times 10^{-3}$  and  $-1.7 \times 10^{-3}$  for  $\epsilon_{yy}$ . Analysis of the strain errors from figure 18 leads to similar conclusions as in the case of the displacements. Gradient methods have a quality advantage over both Newton–Raphson and robust methods for the horizontal and shear strains while the latter perform better for the larger, vertical strains. Using the large blocks produces worse results in the case of the vertical strains because these are highly localized in the central image area and larger block sizes have the tendency to smooth the estimates.

#### 4.4. ‘Plate with hole’ model—large strain analysis

The ‘plate with hole’ displacement model is perfectly adapted for the DIC quality analysis of large strains as well as small strains. In order to create the artificial displacements needed for large strain fields, a new set of parameters was used in the model, with  $E = 0.1$  GPa,  $\nu = 0.5$ , values typical for rubber, the radius of the hole  $a = 200$  pixels and stresses  $\sigma_{xx} = 2$  MPa,  $\sigma_{yy} = 4$  MPa. The resulting displacements have spatial variations very similar to those found in figure 2 but with much larger displacement amplitudes, these ranging from  $-4$  and  $4$  pixels for the horizontal displacements and  $-21.8$  to  $21.8$  pixels for the vertical displacements. The associated theoretical second-order Green–Lagrange strain values varied between  $4.47 \times 10^{-2}$  and  $-2 \times 10^{-2}$  for  $\epsilon_{xx}$ ,  $3.84 \times 10^{-2}$  and  $-3.84 \times 10^{-2}$  for  $\epsilon_{xy}$  and  $9.07 \times 10^{-2}$  and  $-1.02 \times 10^{-2}$  for  $\epsilon_{yy}$ .

In the analysis of the previous cases which referred to small strains, it was clear that large block sizes and linear displacement models present large errors and thus are of little use in practical applications. In dealing with this, for the large strain error analysis, the DIC method parameters were changed to account for larger spatial variations of the strain fields: the block sizes were lowered to  $21 \times 21$ ,  $32 \times 32$  and  $48 \times 48$

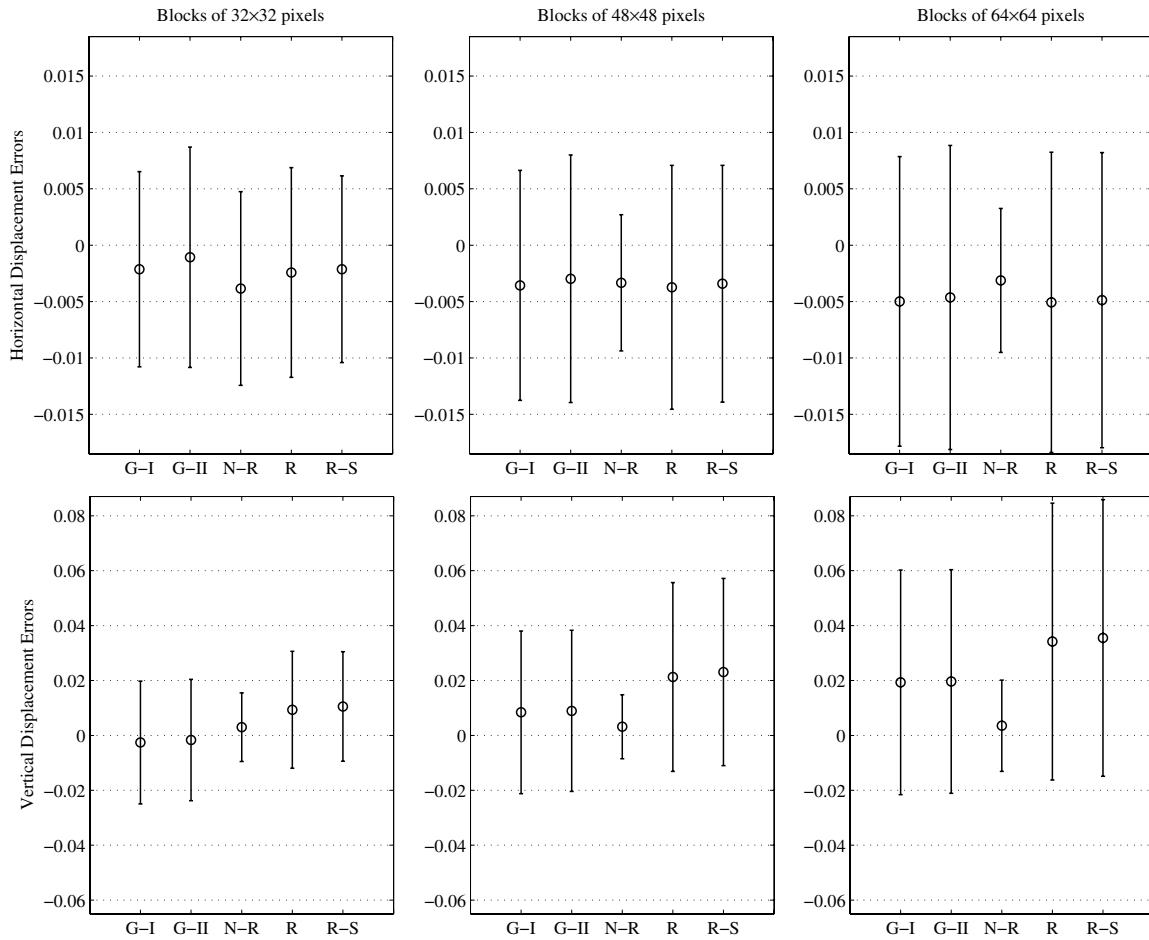


Figure 17. Mean error and standard deviation of the horizontal and vertical displacements for the ‘DIC-based’ displacement model in a  $400 \times 400$  pixel area around the central discontinuity.

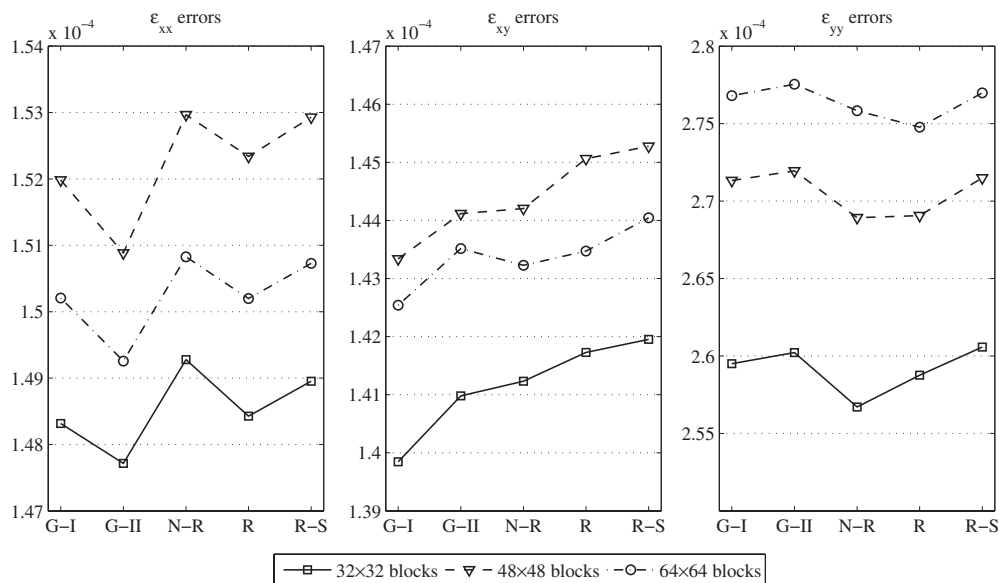
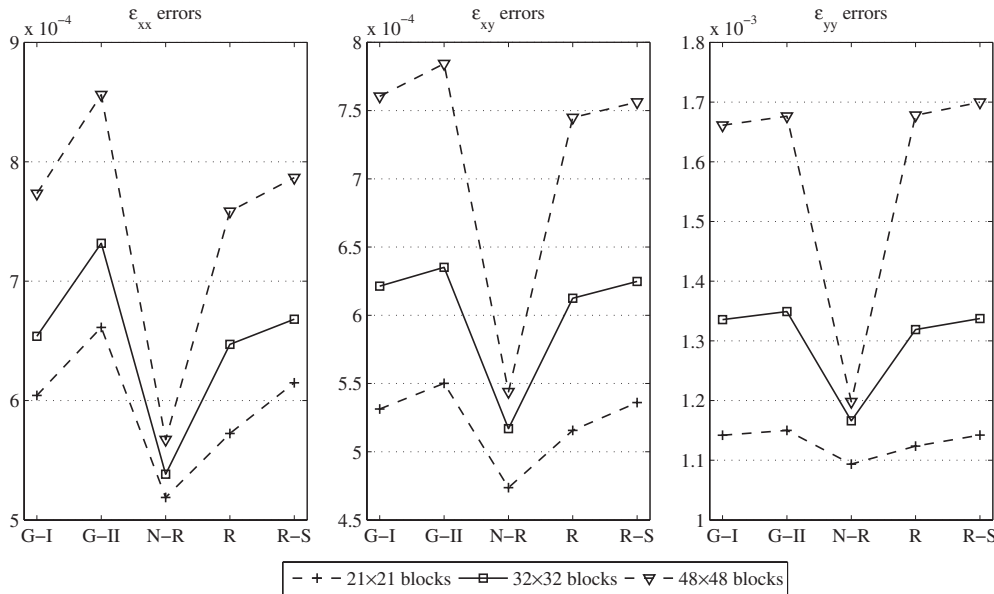


Figure 18. Mean of the absolute strain errors for the ‘DIC-based’ displacement model.

pixels with a 7 pixel step between each two consecutive blocks in the horizontal and vertical directions. The strain window size was kept constant at  $11 \times 11$  displacement locations.

The integer pixel displacements were calculated through block matching with cross-correlation coefficient maximization, the resulting estimates representing the initial solution for the DIC



**Figure 19.** Mean of the absolute large strain errors for the 'plate with hole' model.

methods. The mean absolute errors presented in figure 19 present a large degree of resemblance concerning the relative performance of the DIC algorithms although the errors are larger. As an accuracy reference, the best results were by a large margin given by the Newton–Raphson method with an accuracy ranging from 150 to 500  $\mu\epsilon$  depending on the strain magnitude. The vertical mean errors are larger because of large errors in the strain field corresponding to small areas located above and below the hole where the strains change sign within the span of approximately 30 pixels generating very small strain values. The advantage of the linear displacement model and implicitly the limitations of a translational model are even more apparent when using the  $48 \times 48$  blocks with the mean error for the Newton–Raphson method approximately 50% smaller compared to the other methods. The robust methods performed better, although not significantly, than the gradient ones.

## 5. Conclusion

This paper evaluates five digital image correlation algorithms using artificially warped ground truth images with the known sub-pixel horizontal and vertical motion fields obtained through both theoretical models of material behavior under stress and using motion data from real experiments. The goals of the evaluation were to generate speckle images that simulate deformation processes and insert discontinuities in the motion fields so as to provide a broader view of the advantages and limitations of DIC algorithms while maintaining an elevated degree of realism of the warped picture. The use of the radial basis framework has been investigated both in creating artificial displacements and warping real speckle images in order to obtain the ground truth used in the evaluation process. In the three test cases used, the Newton–Raphson method performed best for the 'plate with hole model' and when large block sizes were used. Regardless of the order of the Taylor

expansion employed, the gradient methods performed very similar and provided accurate results when smaller blocks were used, around areas with motion discontinuities and where the underlying displacements and strains were very small. The robust methods performed with mixed results depending on the nature of the motion present. The robust estimator may impact negatively the quality of the results especially when motion information is highly localized; however, the methods represent a viable DIC alternative when coupled with a good choice of the algorithm parameters. The evaluation suggests two parallel approaches in using DIC methods: using small blocks with a rigid body displacement model when calculating very small displacement or strains or larger blocks and the Newton–Raphson method coupled with more complex motion assumptions for larger strains.

## Appendix A. Gradient method least-squares solutions

Expressing  $g(x + u(x, y), y + v(x, y))$  through a first- or second-order Taylor expansion around  $(x, y)$  and assuming a constant motion model with  $u(x, y) = u_0$  and  $v(x, y) = v_0$  yield

$$g(x + u_0, y + v_0) = g(x, y) + g_x(x, y)u_0 + g_y(x, y)v_0 \quad (\text{A.1})$$

or

$$g(x + u_0, y + v_0) = g(x, y) + g_x(x, y)u_0 + g_y(x, y)v_0 + \frac{1}{2}g_{xx}(x, y)u_0^2 + g_{xy}(x, y)u_0v_0 + \frac{1}{2}g_{yy}(x, y)v_0^2, \quad (\text{A.2})$$

where  $g_x(x, y)$ ,  $g_y(x, y)$ ,  $g_{xx}(x, y)$ ,  $g_{xy}(x, y)$  and  $g_{yy}(x, y)$  are the first- and second-order partial derivatives of the displaced block  $g(x, y)$  with respect to the  $x$  and  $y$  axes.

Depending on the Taylor expansion order presented in equation (A.1) and equation (A.2), the *least-squares*

minimization of equation (1) has the closed form solutions:

$$\begin{bmatrix} u_0 \\ v_0 \end{bmatrix} = \begin{bmatrix} \sum_{x=1}^M \sum_{y=1}^M g_x(x, y)^2 & \sum_{x=1}^M \sum_{y=1}^M g_x(x, y)g_y(x, y) \\ \sum_{x=1}^M \sum_{y=1}^M g_x(x, y)g_y(x, y) & \sum_{x=1}^M \sum_{y=1}^M g_y(x, y)^2 \end{bmatrix}^{-1} \cdot \begin{bmatrix} \sum_{x=1}^M \sum_{y=1}^M (f(x, y) - g(x, y))g_x(x, y) \\ \sum_{x=1}^M \sum_{y=1}^M (f(x, y) - g(x, y))g_y(x, y) \end{bmatrix} \quad (\text{A.3})$$

and, according to Zhang et al [15]

$$\begin{bmatrix} u_0 \\ v_0 \end{bmatrix} = \begin{bmatrix} \sum_{x=1}^M \sum_{y=1}^M (f(x, y) - g(x, y))g_{xx}(x, y) - g_x(x, y)^2 \\ \sum_{x=1}^M \sum_{y=1}^M (f(x, y) - g(x, y))g_{xy}(x, y) - g_x(x, y)g_y(x, y) \\ \sum_{x=1}^M \sum_{y=1}^M (f(x, y) - g(x, y))g_{xy}(x, y) - g_x(x, y)g_y(x, y) \\ \sum_{x=1}^M \sum_{y=1}^M (f(x, y) - g(x, y))g_{yy}(x, y) - g_y(x, y)^2 \end{bmatrix}^{-1} \cdot \begin{bmatrix} \sum_{x=1}^M \sum_{y=1}^M (f(x, y) - g(x, y))g_x(x, y) \\ \sum_{x=1}^M \sum_{y=1}^M (f(x, y) - g(x, y))g_y(x, y) \end{bmatrix}, \quad (\text{A.4})$$

respectively.

### Appendix B. Robust method solution

The solution for the robust error function  $E(u_0, v_0)$  has the general iterative form

$$u_0 = u_0^- - \omega \frac{1}{T(u_0)} \frac{\partial}{\partial u_0} E(u_0, v_0) \quad (\text{B.1})$$

$$v_0 = v_0^- - \omega \frac{1}{T(v_0)} \frac{\partial}{\partial v_0} E(u_0, v_0), \quad (\text{B.2})$$

where  $u_0^-, v_0^-$  are the motion estimates from the previous iteration,  $0 < \omega < 2$  is an over-relaxation parameter and the terms  $T(u_0)$  and  $T(v_0)$  represent an upper bound of the second derivative of  $E$  with respect to the displacements.

The values  $\lambda_D = 1$  and  $\lambda_S = 100$  for the data and smoothness terms were set to perform only mild smoothing, the Lorentzian function parameters were  $\sigma_D = \frac{1}{\sqrt{2}}, \sigma_S = \frac{1}{2}$

and the over-relaxation parameter  $\omega = 1.97$ . Choosing different robust parameters and smoothness term values individually for each of the three test cases and adopting a gradual convexity approach as in [35, 36] may improve the quality and speed over the current choice of parameters which instead provided a good overall compromise.

### Appendix C. RBF interpolation

Considering  $N$  known data points,  $f_i, i = 1, \dots, N$ , with  $(x_i, y_i)$  their plane coordinates, the RBF interpolant at a certain location  $(x, y)$  can be defined as

$$Y(x, y) = \sum_{i=1}^N \lambda_i \Phi(\sqrt{(x - x_i)^2 + (y - y_i)^2}) + p(x, y), \quad (\text{C.1})$$

where  $\lambda_i$  are the RBF expansion coefficients,  $\Phi$  is the chosen radial basis function and  $p(x, y)$  is a low-order polynomial whose presence and order are influenced by the radial basis functions employed. For the functions used here, a first-order polynomial  $p(x, y) = \gamma_1 x + \gamma_2 y + 1$  is sufficient [24].

Solving the interpolation problem by finding RBF parameters  $\lambda_i$  and  $\gamma_{1,2}$  is done by conditioning all the initial data to belong to the interpolant

$$f_i = \sum_{j=1}^{N-1} \lambda_j \Phi(\sqrt{(x_i - x_j)^2 + (y_i - y_j)^2}) + p(x_i, y_i) \quad (\text{C.2})$$

and further adding the polynomial reproduction conditions

$$\sum_{i=1}^N \lambda_i = 0; \quad \sum_{i=1}^N \lambda_i x_i = 0; \quad \sum_{i=1}^N \lambda_i y_i = 0. \quad (\text{C.3})$$

Equation (C.2) and equation (C.3) can be easily put into matrix form and solved using the *least-squares* method, yielding the solution

$$\begin{bmatrix} \lambda_1 \\ \vdots \\ \lambda_N \\ \gamma_1 \\ \gamma_2 \\ 1 \end{bmatrix} = \begin{bmatrix} A_{11} & \cdots & A_{1N} & x_1 & y_1 & 1 \\ \vdots & \ddots & \vdots & \vdots & \vdots & \vdots \\ A_{N1} & \cdots & A_{NN} & x_N & y_N & 1 \\ x_1 & \cdots & x_N & 0 & 0 & 0 \\ y_1 & \cdots & y_N & 0 & 0 & 0 \\ 1 & \cdots & 1 & 0 & 0 & 0 \end{bmatrix}^{-1} \cdot \begin{bmatrix} f_{11} \\ \vdots \\ f_{NN} \\ 0 \\ 0 \\ 0 \end{bmatrix}, \quad (\text{C.4})$$

where  $A_{ij} = \Phi(\sqrt{(x_i - x_j)^2 + (y_i - y_j)^2})$ .

### References

- [1] Sutton M A, Wolters W J, Peters W H and McNeill S R 1983 Determination of displacements using an improved digital correlation method *Image Vision Comput.* **1** 133–9
- [2] Sutton M A, McNeill S R, Jang J S and Babai M 1988 Effects of subpixel image restoration on digital correlation error estimates *Opt. Eng.* **27** 870–7
- [3] Chu T C, Ranson W F and Sutton M A 1985 Applications of digital-image-correlation techniques to experimental mechanics *Exp. Mech.* **25** 232–44
- [4] Chen D J, Chiang F-P, Tan Y S and Don H S 1993 Digital speckle-displacement measurement using a complex spectrum method *Appl. Opt.* **32** 1839–49

- [5] Oriat L and Lantz E 1998 Subpixel detection of the center of an object using a spectral phase algorithm on the image *Pattern Recognit.* **31** 761–71
- [6] Amodio D, Broggiato G B, Campana F and Newaz G M 2003 Digital speckle correlation for strain measurement by image analysis *Exp. Mech.* **43** 396–402
- [7] Van Paepegem W, Shulev A A, Roussev I R, De Pauw S and Degrieck J 2009 Study of the deformation characteristics of window security film by digital image correlation techniques *Opt. Lasers Eng.* **47** 390–7
- [8] Wattrisse B, Chrysochoos A, Muracciole J-M and Nmoz-Gaillard M 2001 Analysis of strain localization during tensile tests by digital image correlation *Exp. Mech.* **41** 29–39
- [9] Lagattu F, Brillaud J and Lafarie-Frenot M-C 2004 High strain gradient measurements by using digital image correlation technique *Mater. Charact.* **53** 17–28
- [10] Bruck H A, McNeill S R, Sutton M A and Peters W H 1989 Digital image correlation using Newton–Raphson method of partial differential correction *Exp. Mech.* **29** 261–7
- [11] Vendroux G and Knauss W G 1998 Submicron deformation field measurements: part 2. Improved digital image correlation *Exp. Mech.* **38** 86–92
- [12] Lu H and Cary P D 2000 Deformation measurements by digital image correlation: implementation of a second-order displacement gradient *Exp. Mech.* **40** 393–400
- [13] Pan B, Xie H, Xu B and Dai F-L 2006 Performance of sub-pixel registration algorithms in digital image correlation *Meas. Sci. Technol.* **17** 1615–21
- [14] Davis C Q and Freeman D M 1998 Statistics of subpixel registration algorithms based on spatiotemporal gradients or block matching *Opt. Eng.* **37** 1290–8
- [15] Zhang J, Jin G, Ma S and Meng L 2003 Application of an improved subpixel registration algorithm on digital speckle correlation measurement *Opt. Laser Technol.* **35** 533–42
- [16] Schreier H W and Sutton M A 2002 Systematic errors in digital image correlation due to undermatched subset shape functions *Exp. Mech.* **42** 303–10
- [17] Cheng P, Sutton M A, Schreier H W and McNeill S R 2002 Full-field speckle pattern image correlation with B-spline deformation function *Exp. Mech.* **42** 344–52
- [18] Bergen J R, Burt P J, Hingorani R and Peleg S 1992 A three-frame algorithm for estimating two-component image motion *IEEE Trans. Pattern Anal. Mach. Intell.* **14** 886–96
- [19] Nunes J C, Bouaoune Y, Delechelle E and Bunel P 2004 A multiscale elastic registration scheme for retinal angiograms *Comput. Vis. Image Underst.* **95** 129–49
- [20] Black M J and Anandan P 1996 The robust estimation of multiple motions: parametric and piecewise-smooth flow fields *Comput. Vis. Image Underst.* **63** 75–104
- [21] Lava P, Cooreman S, Coppeters S, De Strycker M and Debruyne D 2009 Assessment of measuring errors in DIC using deformation fields generated by plastic FEA *Opt. Lasers Eng.* **47** 747–53
- [22] Cárdenas-García J F and Verhaegh J J E 1999 Catalogue of moiré fringes for a bi-axially-loaded infinite plate with a hole *Mech. Research Commun.* **26** 641–8
- [23] Doghri I 2000 *Mechanics of Deformable Solids: Linear and Nonlinear, Analytical and Computational Aspects* (Berlin: Springer)
- [24] De Boer A, Van Der Schoot M S and Bijl H 2007 Mesh deformation based on radial basis function interpolation *Comput. Struct.* **85** 784–95
- [25] Driscoll T A and Heryudono A R H 2007 Adaptive residual subsampling methods for radial basis function interpolation and collocation problems *Comput. Math. Appl.* **53** 927–39
- [26] Sarra S A 2005 Adaptive radial basis function methods for time dependent partial differential equations *Appl. Numer. Math.* **54** 79–94
- [27] Zala C A and Barrodale I 1999 Warping aerial photographs to orthomaps using thin plate splines *Adv. Comput. Math.* **11** 211–27
- [28] Rocha H 2009 On the selection of the most adequate radial basis function *Appl. Math. Modelling* **33** 1573–83
- [29] Arad N, Dyn N, Reisfeld D and Yeshurun Y 1994 Image warping by radial basis functions: application to facial expressions *CVGIP, Graph. Models Image Process.* **56** 161–72
- [30] Siddiqui A M, Masood A and Saleem M 2009 A locally constrained radial basis function for registration and warping of images *Pattern Recognit. Lett.* **30** 377–90
- [31] Jung J-H 2007 A note on the Gibbs phenomenon with multiquadric radial basis functions *Appl. Numer. Math.* **57** 213–29
- [32] Jung J-H and Durante V R 2009 An iterative adaptive multiquadric radial basis function method for the detection of local jump discontinuities *Appl. Numer. Math.* **59** 1449–66
- [33] Perona P and Malik J 1990 Scale-space and edge detection using anisotropic diffusion *IEEE Trans. Pattern Anal. Mach. Intell.* **12** 629–39
- [34] Pan B, Asundi A, Xie H and Gao J 2009 Digital image correlation using iterative least squares and pointwise least squares for displacement field and strain field measurements *Opt. Lasers Eng.* **47** 865–74
- [35] Kim Y-H, Martínez A M and Kak A C 2005 Robust motion estimation under varying illumination *Image Vision Comput.* **23** 365–75
- [36] Blake A and Zisserman A 1987 *Visual Reconstruction* (Cambridge, MA: MIT Press)